

Spatiotemporal Density Correction of Multivariate Global Climate Model Projections using Deep Learning

Reetam Majumder¹, Shiqi Fang², A. Sankarasubramanian²,
Emily C. Hector³, Brian J. Reich³

Abstract

Global Climate Models (GCMs) are numerical models that simulate complex physical processes within the Earth’s climate system and are essential for understanding and predicting climate change. However, GCMs suffer from systemic biases due to simplifications made to the underlying physical processes. GCM output therefore needs to be bias corrected before it can be used for future climate projections. Most common bias correction methods, however, cannot preserve spatial, temporal, or inter-variable dependencies. We propose a new semi-parametric conditional density estimation (SPCDE) for density correction of the joint distribution of daily precipitation and maximum temperature data obtained from gridded GCM spatial fields. The Vecchia approximation is employed to preserve dependencies in the observed field during the density correction process, which is carried out using semi-parametric quantile regression. The ability to calibrate joint distributions of GCM projections has potential advantages not only in estimating extremes, but also in better estimating compound hazards, like heat waves and drought, under potential climate change. Illustration on historical data from 1951–2014 over two 5×5 spatial grids in the US indicate that SPCDE can preserve key marginal and joint distribution properties of precipitation and maximum temperature, and predictions obtained using SPCDE are better calibrated compared to predictions using asynchronous quantile mapping and canonical correlation analysis, two commonly used bias correction approaches.

Key words: Bias correction, Climate modeling, Density correction, Geostatistics, Neural networks, Vecchia approximation.

1 Introduction

Global Climate Models (GCMs) are numerical models to explain complex interactions between the ocean, atmosphere, and land surface. GCMs are used to study long-term climate trends and to provide projections based on possible future scenarios associated with, e.g., greenhouse gas and aerosol emissions, land use, and population growth¹. The latest generation of GCMs are collectively known as the Climate Model Intercomparison Project version 6 (CMIP6; Eyring et al., 2016). It contains the outputs, primarily ocean, atmospheric, and land surface conditions, as ensembles at a coarser spatial scale for further analyzing impacts on various sectors. For instance, GCM forcings, typically precipitation and temperature, are used to assess for both surface water and groundwater availability over the planning period (Singh et al., 2015; Seo et al., 2016). To

¹Department of Mathematical Sciences, University of Arkansas

²Department of Civil, Construction, and Environmental Engineering, North Carolina State University

³Department of Statistics, North Carolina State University

¹<https://www.climate.gov/maps-data/climate-data-primer/predicting-climate/climate-models>

develop these assessments of future water availability, GCM projections, particularly for precipitation and temperature, are forced through hydrologic models, which are subsequently used as an input into a reservoir model (Singh et al., 2015; Seo et al., 2016). Projected inflow into reservoirs are typically used for allocating water for multipurpose uses that includes municipal, irrigation, hydropower and flood control. GCM projections for other variables, particularly temperature and humidity, are also critical for quantifying energy demand (Eshraghi et al., 2021).

Recent computational advances and parameterization of physical processes (e.g., cloud physics) have improved the resolution and accuracy of GCM projections under potential emission scenarios (Ramirez-Villegas et al., 2013; Strandberg and Lind, 2021). Despite these advances, GCM projections have some key drawbacks which need to be addressed before they can be used in climate change impact studies. First, they have systematic biases due to model errors that arise from simplifications made to the underlying physical processes (Stevens and Bony, 2013; Du et al., 2022). These biases lead to discrepancies between observed and model data resulting in an inability to estimate the observed statistics of climate variables (Bhowmik and Sankarasubramanian, 2019). Such discrepancies between modeled and observed data also result in error propagation in sectoral analysis (e.g., water management) (Singh et al., 2015; Seo et al., 2016). In addition, hydrologic projections developed using GCM projections may exhibit uncertainty due to these imprecise forcings (Bhowmik et al., 2017; Seo et al., 2019) or from (long-term) scenarios (Lettenmaier et al., 1999; Hawkins and Sutton, 2011), adding challenges in sectoral application. Second, the coarse resolution of GCMs often fails to fully resolve the effect of topography or sub-grid variability on hydroclimatic variables, especially in projecting precipitation. While some CMIP6 models have a 50 km spatial resolution, most are between 100–250 km. At these resolutions, topography, land use, and land cover are poorly represented; GCMs are therefore unable to accurately capture the land surface and atmospheric feedback that drive local hydroclimatic extremes (Li et al., 2011; O'Brien et al., 2016). These two problems are addressed by bias-correcting and downscaling the GCM output, respectively, carried out over the historical period where both observational and model data are available. The bias correction and downscaling models can then be used to obtain fine-scale, unbiased projections of future climate.

Traditional bias correction methods like quantile mapping (QM) have been used to adjust the distribution of GCM data by mapping quantiles from the GCM to the corresponding quantiles in the observational record (Stoner et al., 2013; Thrasher et al., 2012; Maraun, 2013). While effective for single-variable adjustments, QM often fails to account for inter-variable dependencies (Bhowmik and Sankarasubramanian, 2019). Multivariate bias correction methods aim to preserve the relationships between climatic variables (Bhowmik et al., 2017). While multivariate QMs attempt to address this issue (Piani and Haerter, 2012; Cannon, 2018), QM is inappropriate for the bias correction of future projections as it distorts future climate change in a nonphysical way (e.g., Maurer and Pierce, 2014). Other commonly used methods such as bias corrected spatial downscaling (BCSD, Wood et al., 2002), bias corrected constructed analogues (BCCA, Maurer et al., 2010), and multivariate adapted constructed analogues (MACA, Abatzoglou and Brown, 2012) also employ QM. Multivariate methods like localized constructed analogs (LOCA; Pierce et al., 2014, 2023) and asynchronous canonical correlation analysis (CCA; Bhowmik et al., 2017) offer improvements by better capturing the temporal covariability in climate variables (e.g., cross-correlation), but do

not explicitly consider spatial dependence during bias correction. Finally, recent deep learning-based methods, like DeepSD (Vandal et al., 2017), leverage the power of deep learning algorithms to model complex, nonlinear relationships between climate variables and local geographical information such as elevation, but have not been evaluated for spatiotemporal dependency in multiple climate variables. Additionally, none of the aforementioned methods, with the exception of LOCA v2 (Pierce et al., 2023), are geared towards reproducing observed extreme quantiles of climate variables. However, LOCA v2 also fails to preserve spatial dependency. We argue that bias correction should be viewed as a problem of *density correction* - calibrating the spatiotemporal joint density of the historical GCM projections to the spatiotemporal joint density of the observed multivariate climate data. Subsequently, the ‘calibration’ model will be run with future GCM projections to develop density-corrected (i.e., calibrated) GCM projections that remove the systematic biases in the GCM joint densities. Our effort here is to develop such a density correction approach by comparing the joint density fields of GCM projections with its observed counterpart.

In this paper, we develop a new semi-parametric conditional density estimation (SPCDE) approach for density correction of the joint distribution of daily precipitation (PRCP) and maximum temperature (TMAX) data. The joint distribution of the two variables over a spatial field is decomposed into a product of univariate conditional distributions using a Vecchia approximation (Vecchia, 1988), and each univariate density is estimated using semi-parametric quantile regression (SPQR; Xu and Reich, 2021). SPQR uses neural networks to learn univariate conditional densities of random variables. The deep learning model underpinning SPQR ensures that nonlinear relationships are captured, and the Vecchia approximation ensures that temporal, spatial, and cross correlations are preserved. We test our method with data over twenty five $100 \text{ km} \times 100 \text{ km}$ grid cells in the Southeast and Southwest US, depicted in Figure 1. We use daily data from 1951–2000 to train our density correction model, and data from 2001–2014 to validate our results. Our results indicate that SPCDE is able to preserve key marginal and joint distribution properties of TMAX and PRCP. Additionally, SPCDE predictions are better calibrated over training and testing periods compared to QM and CCA for our spatial domain.

The proposed SPCDE connects conditional density estimation (CDE; Hyndman et al., 1996; Li and Racine, 2006) and bias correction in a unique manner, and in the process mitigates several drawbacks of commonly used bias correction methods. A key aspect of SPCDE (described in further detail in Sections 2.3–2.5) is the estimation of the joint distribution of GCM and observational data within a single SPQR model, and thereafter using cumulative density function (CDF) and quantile function (QF) transforms to calibrate the model data. Similar CDF based approaches have been used for bias correcting future climate projections (e.g., Michelangeli et al., 2009; Li et al., 2010); however, these approaches estimate the CDF of the GCM and observed data independent of each other. SPCDE also bears resemblance to normalizing flows (NFs; Rezende and Mohamed, 2015; Papamakarios et al., 2021; Kobyzev et al., 2021) and transport maps (Marzouk et al., 2016; Katzfuss and Schäfer, 2024). Both of these methods aim to transform a (usually complex) target distribution to a much simpler reference distribution (e.g., a standard Gaussian) through a series of invertible transformations; the transformations are referred to as flows and transport maps, respectively. Inverting the transformations allows for sampling from the target distribution as well as making predictions. Transport maps can be considered a special case of an NF (Katzfuss and

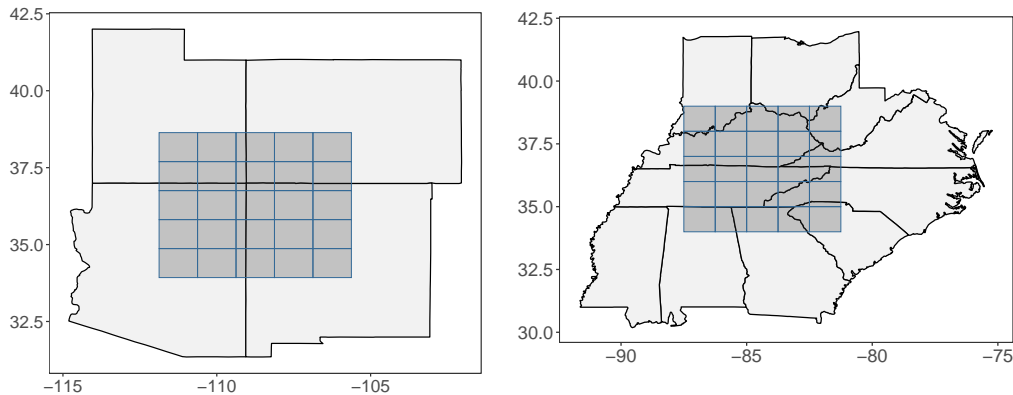


Figure 1: Locations in the Southwest (left) and Southeast (right) regions of the US, which form the basis of our bias-correction case study.

Schäfer, 2024). Similarly, SPCDE parallels NFs - we can consider the GCM and observational data to be distributed according to the reference and target distributions respectively, with the flows being a sequence of CDFs and QFs. This also highlights the key difference between SPCDE and NFs. While the reference distribution in NFs is assumed to be known, the joint distribution of the GCM data also needs to be learned alongside the joint distribution of the observational data. While this is a more complex task, SPCDE’s ability to estimate them simultaneously makes the calibration step of density correction quite straightforward.

The remainder of this paper is organized as follows. Section 2 introduces the data and methods for our study. Section 3 contains a case study for density correction of climate model data at two different regions of the US. Section 4 concludes.

2 Data and Methods

2.1 Overview

Section 2.2 describes the different datasets used in our study, including resolution and pre-processing used to align the different datasets on a common spatial grid. Section 2.3 introduces the SPCDE approach for density correction of TMAX and PRCP at a single grid cell. Sections 2.4 and 2.5 extend SPCDE to spatial and spatiotemporal settings, respectively. Section 2.6 outlines SPQR, the conditional density estimator that is used for SPCDE. Finally, Section 2.7 describes the metrics used to assess the quality of the calibrated data.

2.2 Temperature and precipitation datasets

The study utilizes an ensemble member each from two CMIP6 models - the Geophysical Fluid Dynamics Laboratory (GFDL) GCM, developed by NOAA, and the Max Planck Institute for Meteorology, Germany (MPI) GCM. Both these models provide data at a spatial resolution of $100 \text{ km} \times 100 \text{ km}$, which are used to analyze and density-correct the joint distribution of daily TMAX and PRCP for selected grids in the Southeast US and the Southwest US over the period 1951–2014. The Southwest grid (Figure 1, left panel) spans the states of Utah, Colorado, Arizona, and Mexico, while the Southeast grid (Figure 1, right panel) spans the states of Indiana, Ohio, West Virginia, Kentucky, Virginia, Tennessee, North Carolina, South Carolina, Alabama, and Georgia. The GCM data are obtained from Earth System Grid Federation (ESGF) World Climate Research Programme (WCRP). The primary observational data comes from NOAA’s nClimGrid-daily data product (Vose et al., 2014), which offers daily precipitation and temperature data from 1951 to the present at a $5 \text{ km} \times 5 \text{ km}$ resolution. The observed climate data is aggregated to the same resolution as the GCM data, such that all the datasets used in our study are spatially aligned.

2.3 Density correction model for GCM projections at a single location

Our proposed density correction model has three steps - estimation, projection, and calibration. We begin by stating our model for the general multivariate case in this section; explicit formulations for spatial and spatiotemporal data are described in subsequent sections. We build a statistical model for p continuous responses, $\mathbf{Y} = (Y_1, \dots, Y_p)$ at a single location, which are assumed to have invertible marginal quantile and distribution functions that depends on variables \mathbf{Z} (e.g., season or elevation). The model is described simultaneously for both climate model output and observational data, with an auxiliary variable $X = 0$ indicating the observation is from the climate model and $X = 1$ indicating it is from the observational record.

We write the joint distribution of \mathbf{Y} as a product of univariate conditional distributions

$$f(\mathbf{Y}|\mathbf{Z}, X) = \prod_{j=1}^p f_j(Y_j|\mathbf{Y}_{(j)}, \mathbf{Z}, X), \quad (1)$$

where $\mathbf{Y}_{(j)} = \{Y_i : i \in \mathcal{N}_j\}$ and the conditioning set is $\mathcal{N}_j = \{1, \dots, j-1\}$, which depends on the ordering of the p variables. The responses \mathbf{Y} can alternatively be represented as transformations of the latent variables $\mathbf{U} = (U_1, \dots, U_p)$, with $U_j \stackrel{iid}{\sim} \text{Uniform}(0, 1)$ for $j \in \{1, \dots, p\}$. The map from \mathbf{U} to \mathbf{Y} can be expressed sequentially,

$$Y_j = Q_j(U_j; \mathbf{U}_{(j)}, \mathbf{Z}, X), \quad (2)$$

for $j \in \{1, \dots, p\}$, with $\mathbf{U}_{(j)}$ defined analogous to $\mathbf{Y}_{(j)}$. In (2), Q_j is the univariate conditional quantile function of Y_j given $\mathbf{Y}_{(j)}$, \mathbf{Z} , and X , and thus encapsulates the relationships between the p variables and their dependence on X . Collectively, the transformation is written $\mathbf{Y} = Q(\mathbf{U}; \mathbf{Z}, X)$ with the element j of \mathbf{Y} given by (2).

The inverse map from \mathbf{Y} to \mathbf{U} is determined by the cumulative distribution functions, F_j , corresponding to the Q_j ; i.e., F_j is the inverse function of Q_j , $F_j = Q_j^{-1}$. The inverse map for response

j is

$$U_j = F_j(Y_j; \mathbf{Y}_{(j)}, \mathbf{Z}, X). \quad (3)$$

Collectively, the transformation is written as $\mathbf{U} = F(\mathbf{Y}; \mathbf{Z}, X)$, with the element j of \mathbf{U} determined by (3).

Given the functions F and Q , calibration of climate model output is straightforward. Say \mathbf{Y} is a realization from the climate model, i.e., $X = 0$. Then \mathbf{U} can be computed from (3) as $\mathbf{U} = F(\mathbf{Y}; \mathbf{Z}, 0)$, and the calibrated value for the model variables is then $\mathbf{Y}^* = Q(\mathbf{U}; \mathbf{Z}, 1) = (Y_1^*, \dots, Y_p^*)$. Combining these two steps gives the calibration function C :

$$\mathbf{Y}^* = C(\mathbf{Y}; \mathbf{Z}) := Q\{F(\mathbf{Y}; \mathbf{Z}, 0); \mathbf{Z}, 1\}. \quad (4)$$

If F and Q are correct, then the calibrated climate model output has the same joint distribution as the station data.

While (4) holds for any ordering of the p variables, certain orderings will likely to lead to better estimation depending on the complexity of the p densities. In the simple case of TMAX and PRCP at a single location (i.e., $p = 2$), a natural ordering would be based on choosing Y_1 as TMAX and Y_2 as PRCP. This decomposes the conditional distribution of PRCP and TMAX as a conditional and a marginal distribution, assuming PRCP depends on TMAX. Physically, TMAX and PRCP are coupled, and choosing Y_1 as PRCP and Y_2 as TMAX also provides a valid statistical formulation. However, we assume that PRCP depends on TMAX for somewhat practical reasons. Intuitively, the distribution of TMAX has a much simpler functional form compared to PRCP. PRCP has a preponderance of zeros, and is therefore harder to estimate compared to TMAX. Our proposed dependence structure mitigates this by using TMAX as a predictor for PRCP. Our formulation is also validated in practice; SPCDE where TMAX depended on PRCP led to noticeably worse predictions over both the training and testing periods.

The sequential formulation reduces calibration to estimating the univariate CDFs, F_1, \dots, F_p , sequentially. The function F_j is the conditional CDF of Y_j treating $\mathbf{Y}_{(j)}$, \mathbf{Z} and X as features. These functions can be estimated in parallel with distributional regression methods that allow for a potentially large number of features and flexible relationship between the features and the response distribution. We use semi-parametric quantile regression (SPQR) for the distributional regression which is detailed in Section 2.6. Algorithm 1 summarizes the calibration process for TMAX and PRCP at a single location.

2.4 Extension to spatial data

Consider our problem of interest - density correction of TMAX and PRCP at multiple locations. If there are n locations, a reasonable approach would be to first order them (e.g., based on their geographical coordinates), and then order TMAX and PRCP at each location. This could be represented by $\mathbf{Y} = (Y_1, \dots, Y_p)$ for $p = 2n$, and theoretically, Algorithm 1 from Section 2.3 can be applied. However, as the number of locations increase, so does the number of features $\mathbf{Y}_{(j)}$. This soon leads to computational problems, and directly applying (1) to large spatial (and spatiotemporal) data is computationally prohibitive. To mitigate this, we approximate (1) by means

Algorithm 1 Density correction of $Y_1 = \text{TMAX}$ and $Y_2 = \text{PRCP}$ at a single location

Require: Data $\mathbf{Y}, \mathbf{Z}, X$

procedure SPQR FOR TMAX AND PRCP

Estimate F_1 and Q_1 for $Y_1|\mathbf{Z}, X$

▷ Estimation step

Estimate F_2 and Q_2 for $Y_2|Y_1, \mathbf{Z}, X$

▷ Estimation step

end procedure

procedure TMAX DENSITY CORRECTION

$u_1 \leftarrow F_1(Y_1|X = 0)$

▷ Projection step

$Y_1^* \leftarrow Q_1(u_1|X = 1)$

▷ Calibration step

end procedure

procedure PRCP DENSITY CORRECTION

$\mathbf{Y}_{(2)} \leftarrow Y_1$

$u_2 \leftarrow F_2(Y_2|\mathbf{Y}_{(2)}, X = 0)$

▷ Projection step

$\mathbf{Y}_{(2)}^* \leftarrow Y_1^*$

$Y_2^* \leftarrow Q_2(u_2|\mathbf{Y}_{(2)}^*, X = 1)$

▷ Calibration step

end procedure

of a Vecchia approximation (Vecchia, 1988; Stein et al., 2004; Datta et al., 2016; Katzfuss and Guinness, 2021):

$$f(\mathbf{Y}|\mathbf{Z}, X) = \prod_{j=1}^p f_j(Y_j|Y_{j-1}, \dots, Y_1, \mathbf{Z}, X) \approx \prod_{j=1}^p f_j(Y_j|\mathbf{Y}_{(j)}, \mathbf{Z}, X), \quad (5)$$

where $\mathbf{Y}_{(j)} = \{Y_i; i \in \mathcal{N}_j\}$ and the conditioning set is $\mathcal{N}_j \subseteq \{1, \dots, j-1\}$. We refer to $\mathbf{Y}_{(j)}$ as the *Vecchia neighbor set* going forward. The size of the conditioning set \mathcal{N}_j is therefore bounded above, i.e., $|\mathcal{N}_j| \leq j-1$. In practice, $10 \leq |\mathcal{N}_j| \leq 30$ are often sufficient even when p is very large; we refer the reader to Guinness (2018) and Katzfuss and Guinness (2021) for discussions on optimal choices for cardinality and members of \mathcal{N}_j . The Vecchia approximation facilitates the decomposition of a complex, high-dimensional response vector into a product of independent univariate likelihoods. It is important to note that the approximation is applied only to the dependence structure within \mathbf{Y} , and the right hand expression of (5) is still a valid joint distribution for \mathbf{Y} .

To apply the Vecchia decomposition to the joint distribution of TMAX and PRCP at n locations (with the extension to more than two variables being straightforward), let Y_{1l} and Y_{2l} denote the response for TMAX and PRCP at location $l \in \{1, \dots, n\}$ corresponding to grid point $\mathbf{s}_l = (s_{1l}, s_{2l})$. The $p = 2n$ variables are therefore ordered as $\mathbf{Y} = (Y_{11}, Y_{21}, \dots, Y_{1n}, Y_{2n})$. In this study, we choose the Vecchia neighboring set for Y_{1l} to be $\mathbf{Y}_{(1l)} = \{Y_{1,l-1}, \dots, Y_{1,l-m}\}$, and the Vecchia neighboring set for Y_{2l} as $\mathbf{Y}_{(2l)} = \{Y_{1l}, \dots, Y_{1,l-m}, Y_{2,l-1}, \dots, Y_{2,l-m}\}$. This encapsulates our prior assumption that PRCP depends on TMAX but not vice versa. Therefore, while TMAX at a location depends on TMAX at its Vecchia neighbor locations, PRCP depends on TMAX at the current location and the PRCP at the (same) Vecchia neighbor locations. While other formulations are possible, we found this to be intuitive and tractable.

Algorithm 2 Spatiotemporal density correction for TMAX and PRCP

Require: Data \mathbf{Y}, X

for $l = 1, \dots, n$ **do**

$$\mathbf{Y}_{(1lt)} = \{Y_{1l,t-1}, Y_{1,l-1,t}, \dots, Y_{1,l-m,t}\}$$

$$\mathbf{Y}_{(2lt)} = \{Y_{2l,t-1}, Y_{1l,t-1}, Y_{1lt}, \dots, Y_{1,l-m,t}, Y_{2,l-1,t}, \dots, Y_{2,l-m,t}\}$$

procedure SPQR FOR TMAX AND PRCP

$$\text{Estimate } F_{1l} \text{ and } Q_{1l} \text{ for } Y_{1lt} | \mathbf{Y}_{(1lt)}, X$$

▷ Estimation step

$$\text{Estimate } F_{2l} \text{ and } Q_{2l} \text{ for } Y_{2lt} | \mathbf{Y}_{(2lt)}, X$$

▷ Estimation step

end procedure

procedure TMAX DENSITY CORRECTION

$$u_{1lt} \leftarrow F_{1l}(Y_{1lt} | \mathbf{Y}_{(1lt)}, X = 0)$$

▷ Projection step

for $t = 2, \dots, T$ **do**

$$\mathbf{Y}_{(1lt)}^* = \{Y_{1l,t-1}^*, Y_{1,l-1,t}^*, \dots, Y_{1,l-m,t}^*\}$$

$$Y_{1lt}^* \leftarrow Q_{1l}(u_{1lt} | \mathbf{Y}_{(1lt)}^*, X = 1)$$

▷ Calibration step

end for

end procedure

procedure PRCP DENSITY CORRECTION

$$u_{2lt} \leftarrow F_{2l}(Y_{2lt} | \mathbf{Y}_{(2lt)}, X = 0)$$

▷ Projection step

for $t = 2, \dots, T$ **do**

$$\mathbf{Y}_{(2lt)}^* = \{Y_{2l,t-1}^*, Y_{1l,t-1}^*, Y_{1lt}^*, \dots, Y_{1,l-m,t}^*, Y_{2,l-1,t}^*, \dots, Y_{2,l-m,t}^*\}$$

$$Y_{2lt}^* \leftarrow Q_{2l}(u_{2lt} | \mathbf{Y}_{(2lt)}^*, X = 1)$$

▷ Calibration step

end for

end procedure

end for

2.5 Extension to spatiotemporal data

Finally, we extend the model from Section 2.4 to incorporate temporal information. Let Y_{1lt} and Y_{2lt} denote the response for TMAX and PRCP at location $l \in \{1, \dots, n\}$ and time $t \in \{1, \dots, T\}$. We order the $p = 2nT$ variables as $(Y_{111}, \dots, Y_{11T}, Y_{211}, \dots, Y_{21T}, \dots, Y_{1n1}, \dots, Y_{1nT}, Y_{2n1}, \dots, Y_{2nT})$. The model in Section 2.4 applies to multivariate time series data after key assumptions of Markovian and stationarity dependence structure. The Markovian structure states that the conditional quantile function for Y_{jlt} , $j = 1, 2$, given all observation before time t depends only on data from the previous $T' < T$ time steps; the stationarity assumption states that the conditional quantile functions are invariant to t .

In this study, we assume the conditional quantile function to be first order Markov in time, i.e., $T' = 1$. This assumption is reasonable given the selected are from the Southeast and Southwest US in regions where pronounced seasonality in precipitation is absent (Petersen et al., 2012). This implies that the Vecchia neighbor set for Y_{1lt} is $\mathbf{Y}_{(1lt)} = \{Y_{1l,t-1}, Y_{1,l-1,t}, \dots, Y_{11t}\}$, and for Y_{2lt} is $\mathbf{Y}_{(2lt)} = \{Y_{2l,t-1}, Y_{1l,t-1}, Y_{1,l,t}, \dots, Y_{1,l-m,t}, Y_{2,l-1,t}, \dots, Y_{2,l-m,t}\}$. These are straightforward extensions of the Vecchia neighbor sets presented in Section 2.4, with TMAX on day t being additionally depending on TMAX on day

$t - 1$, and PRCP on day t additionally depending on both PRCP and TMAX from day $t - 1$. The conditional QF Q , CDF F , and calibration function C , for \mathbf{Y}_{lt} are defined identically to Section 2.3; these do not depend on t due to the stationarity assumption. Algorithm 2 details the density correction methodology for spatiotemporal data.

2.6 Conditional density estimation using SPQR

Instead of prescribing parametric forms to the univariate conditional distributions f_j in (1) and (5), we use semi-parametric quantile regression (SPQR, Xu and Reich, 2021) to obtain F , Q , and subsequently, C . For simplicity, in the remainder of this section, we use Y and \mathbf{X} respectively to denote Y_j and $(\mathbf{Y}_{(j)}, X, \mathbf{Z})$ as in (1) and (5). SPQR assumes the PDF of $Y|\mathbf{X}$ to be a function of K second-order M-spline basis functions, $B_1(Y), \dots, B_K(Y)$, with equally-spaced knots spanning $[0, 1]$. Each M-spline basis function is a valid PDF on $[0, 1]$ (Ramsay, 1988), and therefore so are their convex combinations. The SPQR model is

$$f(Y|\mathbf{X}, \phi) = \sum_{k=1}^K \pi_k(\mathbf{X}, \phi) B_k(Y), \quad (6)$$

where the probabilities $\pi_k(\mathbf{X}, \phi)$ function as weights that satisfy $\pi_k(\mathbf{X}, \phi) \geq 0$ and $\sum_{k=1}^K \pi_k(\mathbf{X}, \phi) = 1$, and ϕ are trainable neural network parameters defined below.

By increasing the number of basis functions K and appropriately selecting the weights, the mixture distribution in (6) can approximate any continuous density function (e.g., Chui et al., 1980; Abrahamowicz et al., 1992). To ensure that the weights are chosen in a flexible manner, they are modeled using a multi-layer perceptron (MLP) neural network. The MLP has H hidden layers with rectified linear unit (ReLU, Nair and Hinton, 2010) *activation functions*, which aim to represent nonlinear relationships between the inputs and outputs of each layer. The final layer has a softmax (or equivalently, an expit) activation function, which ensures that the output is a vector of probabilities that sum to 1. The output of layer h is:

$$\mathbf{x}^{(h)} = \text{ReLU}(\mathbf{W}^{(h)} \mathbf{x}^{(h-1)} + \mathbf{b}^{(h)}), \quad h = 1, \dots, H, \quad (7)$$

$$\Pi_K(\mathbf{X}) := \mathbf{x}^{(H+1)} = \text{softmax}(\mathbf{W}^{(H+1)} \mathbf{x}^{(H)} + \mathbf{b}^{(H+1)}), \quad (8)$$

where $\mathbf{x}^{(0)} := \mathbf{X}$ corresponds to the input covariates, and $\Pi_K(\mathbf{X}) = \{\pi_k(\mathbf{X}, \phi)\}_{k=1}^K$ is a K -vector of probabilities that sum to 1. The estimable parameters of the MLP are $\phi = \{\{\mathbf{W}^{(h)}, \mathbf{b}^{(h)}\}_{h=1}^{H+1}\}$, where $\mathbf{W}^{(h)} \in \mathbb{R}^{n_h \times n_{h-1}}$ and $\mathbf{b}^{(h)} \in \mathbb{R}^{n_h}$ are layer-specific weight matrices and bias vectors, respectively. The dimension n_h is referred to as the number of *nodes* in a layer. If we represent each layer operation by a function $g^{(h)}(\cdot)$, suppressing the dependence on ϕ and \mathbf{X} for convenience, the MLP $g : \mathbb{R}^q \rightarrow \mathbb{R}^K$ is a composition of the layer operations, i.e., $g(\cdot) := g^{(H+1)} \circ \dots \circ g^{(1)}(\cdot)$.

The weights and biases in ϕ are optimized through use of stochastic gradient descent with the adaptive moment estimation (Adam) optimizer (Kingma and Ba, 2014); the negative log-likelihood associated with (6) serves as the loss function for the optimization. Computing the PDF is simple and fast given the parameters ϕ . Additionally, the integral of M-spline functions are I-spline functions (Ramsay, 1988), a fact that is exploited to obtain an expression for the cumulative distribution

function (CDF):

$$F(Y|\phi, \mathbf{X}) = \sum_{k=1}^K \pi_k(\mathbf{X}, \phi) I_k(Y), \quad (9)$$

where $I_k(Y)$ are I-spline basis functions. The conditional quantile function for quantile level $\tau \in (0, 1)$ is defined as the function $Q(\tau|\phi, \mathbf{X})$ so that

$$F\{Q(\tau|\phi, \mathbf{X})|\phi, \mathbf{X}\} = \tau.$$

The conditional quantile function for this model is not available in closed-form, but can be approximated by numerically inverting $F(Y|\phi, \mathbf{X})$. Given that (9) models a valid CDF, the conditional quantile function estimated through this approach satisfies the non-crossing constraint

$$\frac{\partial Q(\tau|\phi, \mathbf{X})}{\partial \tau} > 0, \quad \forall \mathbf{X},$$

and does not require any second-stage monotization treatment (Bondell et al., 2010).

2.7 Model evaluation metrics for SPCDE

In the study presented in Section 3, we assess the efficacy of SPCDE based on five functionals of the joint distribution of TMAX and PRCP: the Wasserstein distance between the marginal densities of calibrated and observational data, lag-1 autocorrelations, pairwise spatial correlations, and their 0.95 quantiles. These are evaluated for both the observed (nClimGrid) and calibrated predictions. We also evaluated the proportion of zeros for PRCP, and the cross correlation between TMAX and PRCP. The Wasserstein distance (Kantorovich, 1960; Vasershtein, 1969) quantifies the overall fit of the marginal distributions of each variable in terms of the dissimilarity between the densities of the observed and calibrated data, whereas the proportion of zeros and the 0.95 quantiles focus specifically on the tail behavior of the distributions. The three correlation metrics ensure that the calibrated data maintains the dependence structure of the nClimGrid data.

In addition to assessing goodness of fit of our density corrected data, we also compare it with QM and CCA. As described in Section 1, QM is a bias correction method which matches the quantiles of the observational data time series and the GCM time series. The asynchronous QM bias correction method sorts GCM and nClimGrid data vectors in ascending order (independently), and then fits linear regression to the sorted data. This can take the form of simple linear regression (e.g., Dettinger et al., 2004) or piecewise linear regression (Stoner et al., 2013). The QM methodology is applied separately for each month, grid cell, and variable (TMAX and PRCP). The goal is to obtain a linear map between the quantiles of the GCM and nClimGrid datasets. We can then provide GCM data for unobserved grid points or time periods as input to the fitted model and obtain bias-corrected TMAX and PRCP as output. The resulting values must subsequently be rearranged back into the original order to retrieve the final product, a continuous chronological time series of the bias-corrected values. Since QM in our example is applied to each variable separately, it fails to account for inter-variable dependencies (Bhowmik and Sankarasubramanian, 2019). This can distort relationships critical for understanding processes such as hydrological cycles (Seo et al.,

2019). We use CCA (Bhowmik et al., 2017) as our other point of comparison. CCA employs multivariate sorting of variables based on their joint probability of occurrence such that their cross correlation is maintained. Afterwards, canonical correlation is used to bias correct variables simultaneously. Neither of these two approaches, however, explicitly models spatial or temporal dependence present in the data.

3 Density correction of historical TMAX and PRCP

3.1 Overview

We implemented SPCDE for daily observational and GCM data from 1951–2014 on two separate 5×5 grids as shown in Figure 1. We separated the data into a training period (1951–2000) and a testing period (2001–2014), and fitted the spatiotemporal SPCDE model to the training period data. The Vecchia neighbor sets are selected using max-min ordering, which can result in significant improvements over other coordinate based orderings (Guinness, 2018). We model each month’s data separately to account for seasonality. Additionally, since daily PRCP contains a large proportion of zeroes and SPQR does not work with semi-continuous data, we do not model PRCP directly. Instead, we model $\log(0.0001 + \text{PRCP})$, a common approach when modeling precipitation data using continuous distributions (Rajagopalan and Lall, 1998). We found this transformation sufficient for the simultaneous estimation of the proportion of zeros in the data, combined with a post-processing step (described in Section 3.2), as well as high quantiles.

For each month and at every location conditioned on its neighboring set of locations, we fitted SPQR models for TMAX and the transformed PRCP. Each SPQR model has several hyperparameters, which were chosen based on a grid search based on different hyperparameter values (not presented). We choose each SPQR model to have 2 hidden layers with 30 and 20 nodes, and 20 output knots for both variables. The batch size and learning rate is set to 100 and 0.001 respectively, and the SPQR model is run for 300 iterations. In each model, 20% of the training data is used as a validation set, with early stopping enforced if the validation set loss fails to decrease for more than 5 iterations.

The SPQR models (for each month, location, and variable) can be fit in parallel, since the Vecchia approximation decomposes the joint density of \mathbf{Y} into independent univariate conditional densities. Predictions for every month can also be carried out independently, and therefore the projection/calibration step occurs in parallel. Within each month, however, predictions need to be made in the same sequence as the ordering of the Vecchia neighbor sets. Predictions for TMAX and PRCP were obtained for the testing period of 2001–2014 at each location using Algorithm 2.

3.2 Evaluating bias-corrected output based on SPCDE

We first present results from density correction at both sets of locations for the validation period of 2001–2014. Figure 2 plots density curves of density corrected TMAX and log-scale PRCP for the SE and SW regions. Each curve pools the entire validation period data across all 25 locations, and we see that the calibrated TMAX and PRCP closely match the observed data. Note that the density

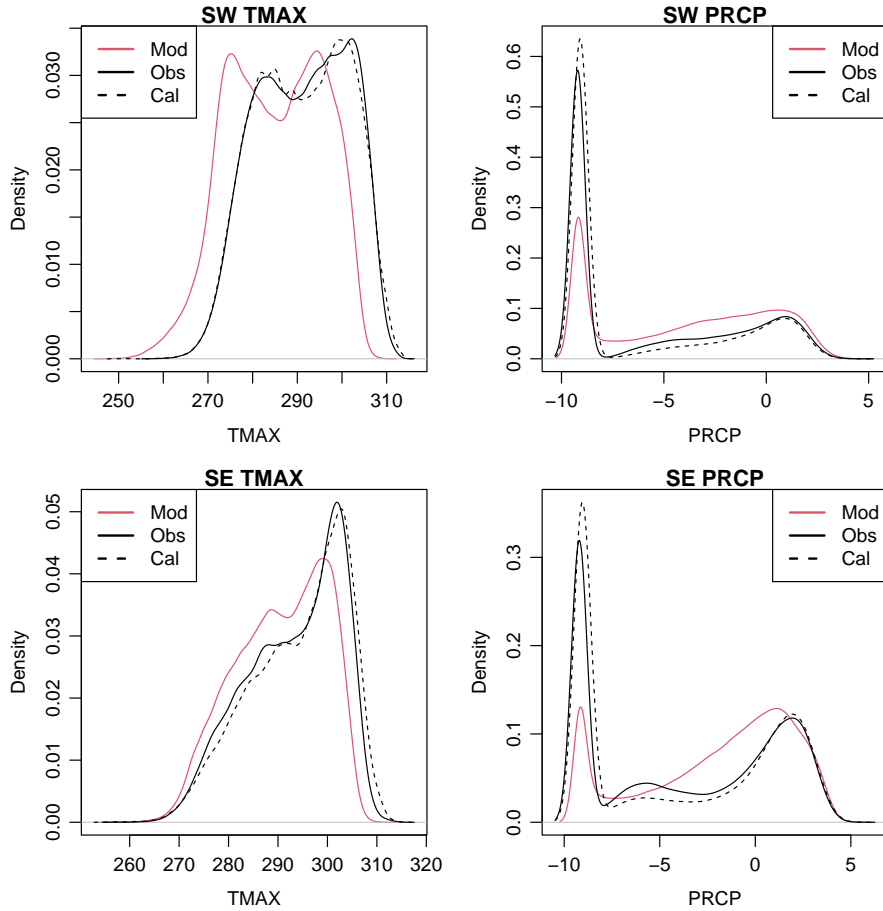


Figure 2: Density curves of climate model (Mod), observed (Obs), and calibrated (Cal) TMAX and PRCP data in the Southwest (SW) and Southeast (SE) average over location and month from 2001–2014. PRCP results are presented in the log scale.

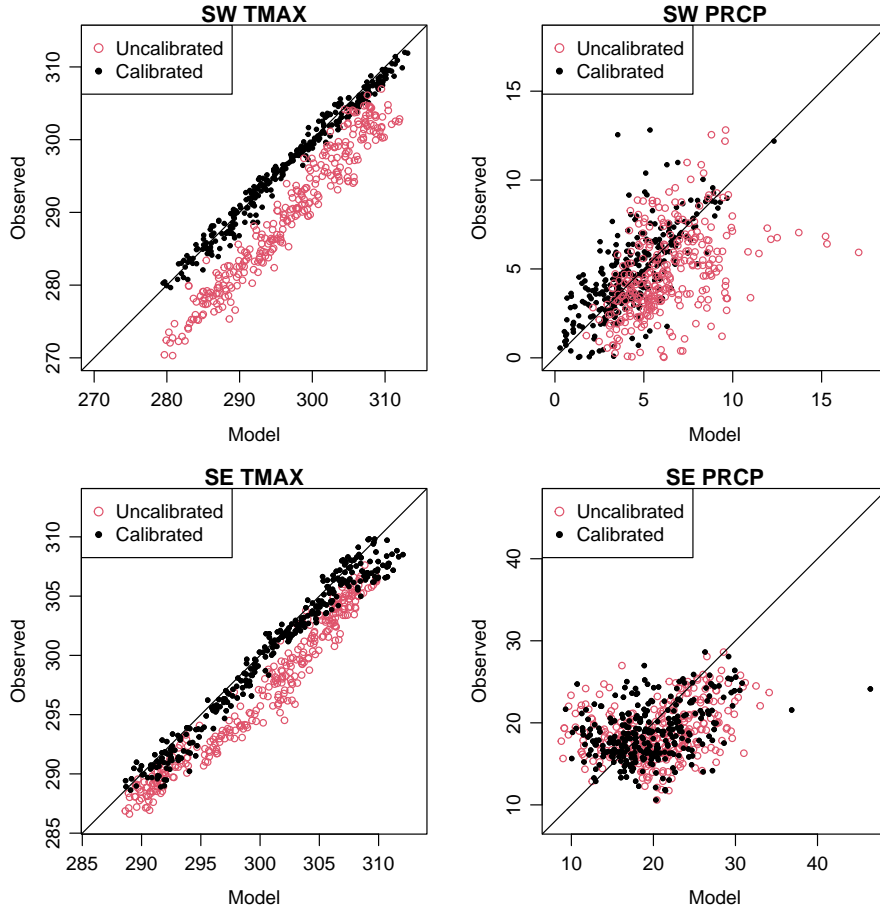


Figure 3: Monthly 0.95 quantiles of TMAX and PRCP data in the Southwest (SW) and Southeast (SE), aggregated over 2001–2014. Each point corresponds to a particular month and location.

plots for PRCP are displayed in the transformed log scale since visual inspection of the density plots are most informative in the scale that the data was analyzed. However, all remaining plots and metrics for PRCP are presented in the raw data scale. Fitting separate monthly models for TMAX captures the pronounced bimodal distribution in the SW region with different modes for observed and model data. On the other hand, there are substantial differences between the observed and model densities of PRCP at both tails of their respective distributions. For both variables, SPQR is able to successfully calibrate the model data to match the density of the observational data.

Figures 3–4 plot the 0.95 quantiles of TMAX and PRCP, and the proportion of zeros for PRCP, respectively. Each panel displays the effect of density correction by comparing it against the observational data for every location and month. For the upper 0.95 quantiles, the uncalibrated model values for TMAX have noticeable bias, something that can be visually verified in Figure 2. The calibrated quantiles virtually eliminates this bias while also having lower uncertainty than the uncalibrated data. The density correction also improves upper quantile estimation for PRCP. However, it is unable to fully adjust for the bias, and there is noticeably more uncertainty in the PRCP

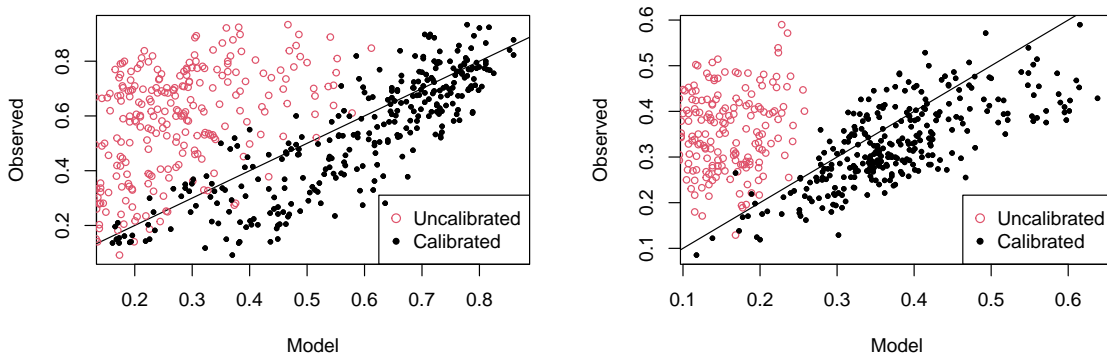


Figure 4: Monthly Proportion of zeros in PRCP data for the Southwest (SW) and Southeast (SE), aggregated over 2001–2014. Each point corresponds to a particular month and location.

estimates than TMAX. Part of this bias is attributable to the proportion of zeros in PRCP data, which varies significantly by season. We therefore treat model precipitation below 0.001 mm as zero precipitation, since it is not measurable by physical instruments like rain gauges. This was also done for the SPQR estimates since the continuous fitted distribution for PRCP will never produce exact zeros. The uncalibrated model data (red) in Figure 4 severely underestimates the proportion of zeros, due to a well known phenomenon called the *drizzle effect* (see, e.g., Levey and Sankarasubramanian, 2024), where numerical climate models for precipitation very rarely generate zero precipitation values, instead usually having very small but positive values. The calibrated density of PRCP is able to accurately represent the proportion of zeros that are observed in the real data, indicating that our log-transform for modeling PRCP is adequate for this application.

Figures 5–6 plot the effect of density correction on the autocorrelations for each variable, and the cross correlation between them, respectively. As in the previous two plots, points correspond to month and location specific estimates. In Figure 5, SPCDE is unable to improve the autocorrelation for SW TMAX from its model values, but for the remaining three variables, the calibrated data has lower bias and variability in its estimates of autocorrelation compared to the uncalibrated model data. For the cross correlations in Figure 6, the uncalibrated data has positive bias in the cross correlations for both regions. Density correction was able to virtually eliminate the bias and provided highly accurate and precise estimates of the cross correlation. This is in part because the conditional density of PRCP depends on both current and past TMAX values, and therefore SPQR models the dependence between the two variables.

Finally, Figure 7 shows pairwise spatial correlations for the calibrated and uncalibrated data. Each panel contains values for 300 pairs of locations. Values are concentrated around the diagonal, suggesting the the calibrated data has similar spatial correlation compared to the observed data. We do notice more uncertainty in the lower end of TMAX correlation values in the uncalibrated data, that the density correction is not able to entirely address, but overall the calibrated data has lower bias and uncertainty compared to the uncalibrated model data.

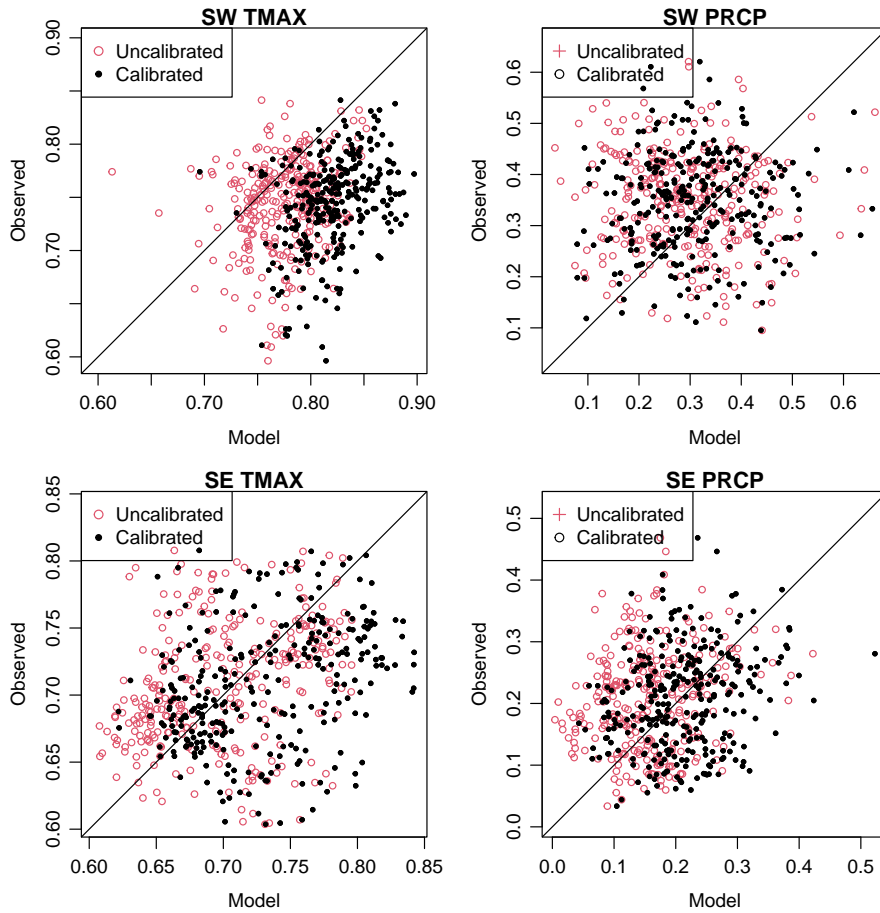


Figure 5: Monthly lag-1 autocorrelations of TMAX and PRCP data in the Southwest (SW) and Southeast (SE), aggregated over 2001–2014. Each point corresponds to a particular month and location.

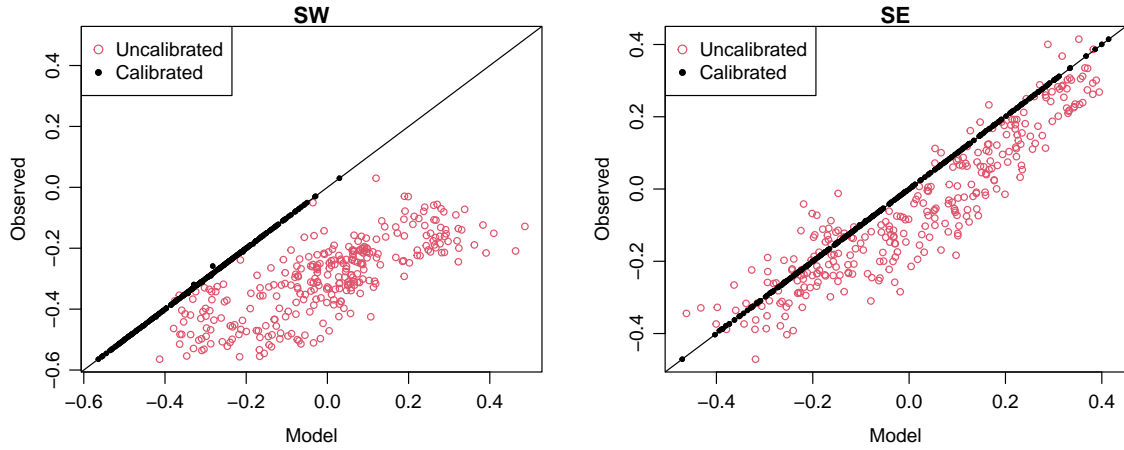


Figure 6: Monthly cross-correlations between TMAX and PRCP in the Southwest (SW) and South-east (SE), aggregated over 2001–2014. Each point corresponds to a particular month and location.

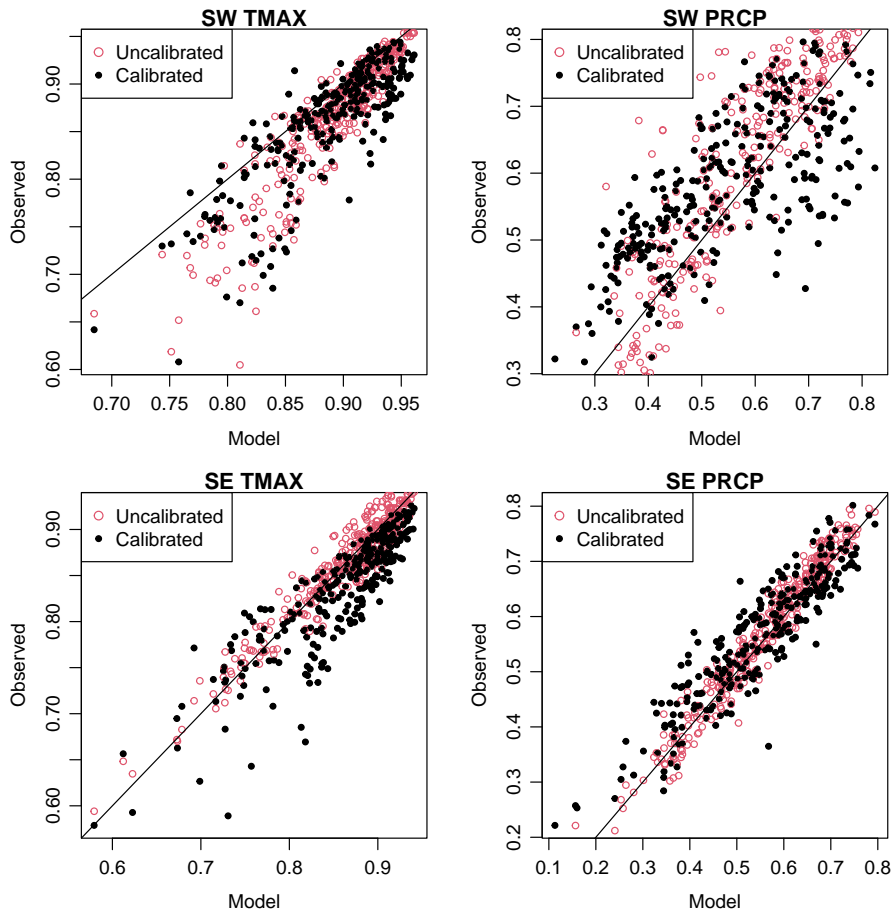


Figure 7: Annual spatial correlations of TMAX and PRCP data in the Southwest (SW) and South-east (SE), aggregated over 2001–2014. Each point corresponds to a pair of locations.

Table 1: Out-of-sample prediction accuracy in the density correction of TMAX and PRCP based on a spatiotemporal SPCDE model, compared with canonical correlation analysis (CCA) and quantile mapping (QM). Other than the Wasserstein distance metric, the remaining values correspond to the RMSE between observed and calibrated data for 2001–2014. Metrics are averaged across spatial locations (pairs of locations for spatial correlation). Best (smallest) values for each combination of region, variable, and metric are highlighted.

		Southwest			Southeast		
		SPCDE	CCA	QM	SPCDE	CCA	QM
TMAX	Wasserstein distance	0.3001	0.9270	0.3073	1.0377	1.3454	1.6735
	0.95 quantile	1.2225	0.9202	1.1136	1.4198	1.7515	2.2220
	Lag-1 autocorrelation	0.0878	0.6873	0.6340	0.0617	0.6768	0.6261
	Spatial correlation	0.0567	0.0737	0.0670	0.0231	0.0653	0.0639
PRCP	Wasserstein distance	0.1049	0.5427	0.1256	0.3057	0.8573	0.4780
	0.95 quantile	1.7358	2.3285	1.6520	4.9077	4.9544	5.8247
	Proportion of zeros	0.1222	0.2111	0.2227	0.0818	0.1056	0.1978
	Lag-1 autocorrelation	0.1441	0.4102	0.3539	0.0970	0.2978	0.2362
	Spatial correlation	0.1205	0.1281	0.1283	0.0528	0.1401	0.1382
	Cross correlation	0.0017	0.3209	0.3209	0.0006	0.1039	0.1039

3.3 Comparison of SPCDE with CCA and QM

To evaluate the performance of the SPCDE density correction approach compared to CCA and QM, we provide metrics for predictive accuracy based on the three methods in Table 1. Marginal fits for TMAX and the transformed PRCP are summarized using the Wasserstein distance, while for the remainder of the metrics provided in this section, we evaluate the RMSE. In each case, smaller values indicate more accurate predictions. We note that the SPCDE predictions are better than CCA and QM predictions across the board. The only two instances where SPCDE is not outright better are the 0.95 quantiles for SW TMAX and PRCP. Neither CCA nor QM is clearly better even in this case, with the former having lower RMSE for TMAX, and the latter having a lower RMSE for PRCP. On the other hand, SPCDE is still the best among the three methods at estimating the proportion of zeros in PRCP for both regions. The autocorrelations are also significantly better for SPCDE, since neither of the competing method explicitly accounts for autocorrelation. While SPCDE has smaller RMSE for spatial correlations in every case, the differences are more noticeable for the SE, which has both lower bias and variability in its spatial correlation estimates (see Figure 7). Finally, RMSE in the cross correlations are around 3 three orders of magnitude smaller for SPCDE than competing methods.

Overall, the SPCDE calibrated distributions of TMAX and PRCP have the same characteristics as their observed data counterparts, for statistics of interest. In particular, it is able to very accurately capture the relationship between the two variables, which is crucial as they jointly affect several quantities of practical interest, including droughts, fire risk, and streamflow.

4 Discussion

In this paper, we develop a new SPCDE approach for the simultaneous density correction of spatiotemporal PRCP and TMAX. A key goal of our study is to maintain the cross correlation between the two variables during density correction. SPCDE leverages the Vecchia approximation to maintain spatiotemporal and inter-variable dependencies, and density estimation is carried out using the deep learning based SPQR method. Our approach is trained across two spatial fields in the Southeast and Southwest US using historical data from 1951–2000, and tested using data from 2001–2014 for the same region. SPCDE is able to outperform QM and CCA, two competing methods, and the joint distribution characteristics of the observational data is preserved in the bias-corrected data.

SPCDE is highly scalable, since the Vecchia approximation allows for fitting models at different locations and months in parallel. Additionally, it ensures that the computational cost is linear in the number of grid cells. In our current implementation, however, we fit separate models for each month so that seasonality does not affect our results. Future work will focus on consolidating the monthly models into a single annual model to reduce computational cost and improve estimation (since significantly more data will be available to train the annual model). We anticipate this can be achieved by including more time-based covariates to account for trends and seasonality, in a way that improves the estimation of autocorrelation in the data. Additionally, we plan to extend SPQR to support a bivariate response variable, which could then be used to directly model the joint distribution of TMAX and PRCP without needing to decompose it into a product of a conditional and a marginal distribution. The ultimate goal of these anticipated extensions is to provide future projections of TMAX and PRCP across the entire contiguous US.

Acknowledgements

This work was supported by a grant from the National Science Foundation (DMS 2152887, CBET 2151651). Hector was also supported by an Internationalization Seed Grant award from the Office of Global Engagement at North Carolina State University.

References

- Abatzoglou, J. T. and Brown, T. J. (2012) A comparison of statistical downscaling methods suited for wildfire applications. *International Journal of Climatology*, **32**, 772–780.
- Abrahamowicz, M., Clapml, A. and Ramsay, J. O. (1992) Nonparametric density estimation for censored survival data: Regression-spline approach. *Canadian Journal of Statistics*, **20**, 171–185.
- Bhowmik, R. D. and Sankarasubramanian, A. (2019) Limitations of univariate linear bias correction in yielding cross-correlation between monthly precipitation and temperature. *International Journal of Climatology*, **39**, 4479–4496.
- Bhowmik, R. D., Sankarasubramanian, A., Sinha, T., Patskoski, J., Mahinthakumar, G. and Kunkel, K. E. (2017) Multivariate downscaling approach preserving cross correlations across climate variables for projecting hydrologic fluxes. *Journal of Hydrometeorology*, **18**, 2187 – 2205.
- Bondell, H. D., Reich, B. J. and Wang, H. (2010) Noncrossing quantile regression curve estimation. *Biometrika*, **97**, 825–838.
- Cannon, A. J. (2018) Multivariate quantile mapping bias correction: an n-dimensional probability density function transform for climate model simulations of multiple variables. *Climate Dynamics*, **50**, 31–49.
- Chui, C., Smith, P. and Ward, J. (1980) Degree of L_p approximation by monotone splines. *SIAM Journal on Mathematical Analysis*, **11**, 436–447.
- Datta, A., Banerjee, S., Finley, A. O. and Gelfand, A. E. (2016) Hierarchical nearest-neighbor Gaussian process models for large geostatistical datasets. *Journal of the American Statistical Association*, **111**, 800–812.
- Dettinger, M. D., Cayan, D. R., Meyer, M. K. and Jeton, A. E. (2004) Simulated hydrologic responses to climate variations and change in the merced, carson, and american river basins, sierra nevada, california, 1900–2099. *Climatic Change*, **62**, 283–317.
- Du, Y., Wang, D., Zhu, J., Wang, D., Qi, X. and Cai, J. (2022) Comprehensive assessment of cmip5 and cmip6 models in simulating and projecting precipitation over the global land. *International Journal of Climatology*, **42**, 6859–6875.
- Eshraghi, H., Rodrigo de Queiroz, A., Sankarasubramanian, A. and DeCarolis, J. F. (2021) Quantification of climate-induced interannual variability in residential u.s. electricity demand. *Energy*, **236**, 121273.
- Eyring, V., Bony, S., Meehl, G. A., Senior, C. A., Stevens, B., Stouffer, R. J. and Taylor, K. E. (2016) Overview of the coupled model intercomparison project phase 6 (cmip6) experimental design and organization. *Geosci. Model Dev.*, **9**, 1937–1958.

- Guinness, J. (2018) Permutation and grouping methods for sharpening Gaussian process approximations. *Technometrics*, **60**, 415–429.
- Hawkins, E. and Sutton, R. (2011) The potential to narrow uncertainty in projections of regional precipitation change. *Climate Dynamics*, **37**, 407–418.
- Hyndman, R. J., Bashtannyk, D. M. and Grunwald, G. K. (1996) Estimating and visualizing conditional densities. *Journal of Computational and Graphical Statistics*, **5**, 315–336.
- Kantorovich, L. V. (1960) Mathematical methods of organizing and planning production. *Problems Inform. Transmission*, **6**, 366–422.
- Katzfuss, M. and Guinness, J. (2021) A general framework for Vecchia approximations of Gaussian processes. *Statistical Science*, **36**, 124–141.
- Katzfuss, M. and Schäfer, F. (2024) Scalable bayesian transport maps for high-dimensional non-gaussian spatial fields. *Journal of the American Statistical Association*, **119**, 1409–1423.
- Kingma, D. P. and Ba, J. (2014) Adam: A method for stochastic optimization. *arXiv preprint arXiv:1412.6980*.
- Kobyzev, I., Prince, S. J. and Brubaker, M. A. (2021) Normalizing flows: An introduction and review of current methods. *IEEE Transactions on Pattern Analysis and Machine Intelligence*, **43**, 3964–3979.
- Lettenmaier, D. P., Wood, A. W., Palmer, R. N., Wood, E. F. and Stakhiv, E. Z. (1999) Water resources implications of global warming: A u.s. regional perspective. *Climatic Change*, **43**, 537–579.
- Levey, J. R. and Sankarasubramanian, A. (2024) Spatial and temporal variation of subseasonal-to-seasonal (s2s) precipitation reforecast skill across the conus. *Journal of Hydrometeorology*, **25**, 755 – 770.
- Li, F., Collins, W. D., Wehner, M. F., Williamson, D. L., Olson, J. G. and Algieri, C. (2011) Impact of horizontal resolution on simulation of precipitation extremes in an aqua-planet version of community atmospheric model (cam3). *Tellus A: Dynamic Meteorology and Oceanography*.
- Li, H., Sheffield, J. and Wood, E. F. (2010) Bias correction of monthly precipitation and temperature fields from intergovernmental panel on climate change ar4 models using equidistant quantile matching. *Journal of Geophysical Research: Atmospheres*, **115**.
- Li, Q. and Racine, J. S. (2006) *Nonparametric Econometrics: Theory and Practice*, vol. 1 of *Economics Books*. Princeton University Press.
- Maraun, D. (2013) Bias correction, quantile mapping, and downscaling: Revisiting the inflation issue. *Journal of Climate*, **26**, 2137 – 2143.

- Marzouk, Y., Moselhy, T., Parno, M. and Spantini, A. (2016) *Sampling via Measure Transport: An Introduction*, 1–41. Cham: Springer International Publishing.
- Maurer, E. P., Hidalgo, H. G., Das, T., Dettinger, M. D. and Cayan, D. R. (2010) The utility of daily large-scale climate data in the assessment of climate change impacts on daily streamflow in california. *Hydrology and Earth System Sciences*, **14**, 1125–1138.
- Maurer, E. P. and Pierce, D. W. (2014) Bias correction can modify climate model simulated precipitation changes without adverse effect on the ensemble mean. *Hydrology and Earth System Sciences*, **18**, 915–925. URL <https://hess.copernicus.org/articles/18/915/2014/>.
- Michelangeli, P.-A., Vrac, M. and Loukos, H. (2009) Probabilistic downscaling approaches: Application to wind cumulative distribution functions. *Geophysical Research Letters*, **36**.
- Nair, V. and Hinton, G. E. (2010) Rectified linear units improve restricted boltzmann machines. In *Proceedings of the 27th International Conference on International Conference on Machine Learning*, ICML'10, 807–814. Madison, WI, USA: Omnipress.
- O'Brien, T. A., Collins, W. D., Kashinath, K., Rübel, O., Byna, S., Gu, J., Krishnan, H. and Ullrich, P. A. (2016) Resolution dependence of precipitation statistical fidelity in hindcast simulations. *Journal of Advances in Modeling Earth Systems*, **8**, 976–990.
- Papamakarios, G., Nalisnick, E., Rezende, D. J., Mohamed, S. and Lakshminarayanan, B. (2021) Normalizing flows for probabilistic modeling and inference. *J. Mach. Learn. Res.*, **22**.
- Petersen, T., Devineni, N. and Sankarasubramanian, A. (2012) Seasonality of monthly runoff over the continental united states: Causality and relations to mean annual and mean monthly distributions of moisture and energy. *Journal of Hydrology*, **468–469**, 139–150.
- Piani, C. and Haerter, J. O. (2012) Two dimensional bias correction of temperature and precipitation copulas in climate models. *Geophysical Research Letters*, **39**.
- Pierce, D. W., Cayan, D. R., Feldman, D. R. and Risser, M. D. (2023) Future increases in north american extreme precipitation in CMIP6 downscaled with LOCA. *Journal of Hydrometeorology*, **24**, 951 – 975.
- Pierce, D. W., Cayan, D. R. and Thrasher, B. L. (2014) Statistical downscaling using localized constructed analogs (LOCA). *Journal of Hydrometeorology*, **15**, 2558 – 2585.
- Rajagopalan, B. and Lall, U. (1998) Locally weighted polynomial estimation of spatial precipitation. *Journal of Geographic Information and Decision Analysis*, **2**, 44–51.
- Ramirez-Villegas, J., Challinor, A. J., Thornton, P. K. and Jarvis, A. (2013) Implications of regional improvement in global climate models for agricultural impact research. *Environmental Research Letters*, **8**, 024018.

- Ramsay, J. O. (1988) Monotone regression splines in action. *Statistical Science*, 425–441.
- Rezende, D. J. and Mohamed, S. (2015) Variational inference with normalizing flows. In *Proceedings of the 32nd International Conference on International Conference on Machine Learning - Volume 37, ICML'15*, 1530–1538. JMLR.org.
- Seo, S., Das Bhowmik, R., Sankarasubramanian, A., Mahinthakumar, G. and Kumar, M. (2019) The role of cross-correlation between precipitation and temperature in basin-scale simulations of hydrologic variables. *Journal of Hydrology*, **570**, 304–314.
- Seo, S. B., Sinha, T., Mahinthakumar, G., Sankarasubramanian, A. and Kumar, M. (2016) Identification of dominant source of errors in developing streamflow and groundwater projections under near-term climate change. *Journal of Geophysical Research: Atmospheres*, **121**, 7652–7672.
- Singh, H., Sinha, T. and Sankarasubramanian, A. (2015) Impacts of near-term climate change and population growth on within-year reservoir systems. *Journal of Water Resources Planning and Management*, **141**, 04014078.
- Stein, M. L., Chi, Z. and Welty, L. J. (2004) Approximating likelihoods for large spatial data sets. *Journal of the Royal Statistical Society: Series B (Statistical Methodology)*, **66**, 275–296.
- Stevens, B. and Bony, S. (2013) What are climate models missing? *Science*, **340**, 1053–1054.
- Stoner, A. M. K., Hayhoe, K., Yang, X. and Wuebbles, D. J. (2013) An asynchronous regional regression model for statistical downscaling of daily climate variables. *International Journal of Climatology*, **33**, 2473–2494.
- Strandberg, G. and Lind, P. (2021) The importance of horizontal model resolution on simulated precipitation in europe – from global to regional models. *Weather and Climate Dynamics*, **2**, 181–204.
- Thrasher, B., Maurer, E. P., McKellar, C. and Duffy, P. B. (2012) Technical note: Bias correcting climate model simulated daily temperature extremes with quantile mapping. *Hydrology and Earth System Sciences*, **16**, 3309–3314.
- Vandal, T., Kodra, E., Ganguly, S., Michaelis, A. R., Nemani, R. R. and Ganguly, A. R. (2017) DeepSD: Generating high resolution climate change projections through single image super-resolution. *CoRR*, **abs/1703.03126**. URL <http://arxiv.org/abs/1703.03126>.
- Vasershtein, L. N. (1969) Markov processes over denumerable products of spaces describing large system of automata. *Problems Inform. Transmission*, **5**, 47–52.
- Vecchia, A. V. (1988) Estimation and model identification for continuous spatial processes. *Journal of the Royal Statistical Society: Series B (Methodological)*, **50**, 297–312.

- Vose, R. S., Applequist, S., Squires, M., Durre, I., Menne, M. J., Williams Jr., C. N., Fenimore, C., Gleason, K. and Arndt, D. (2014) NOAA Monthly U.S. Climate Gridded Dataset (NClimGrid), Version 1. NOAA National Centers for Environmental Information, DOI:10.7289/V5SX6B56, accessed on Nov 1, 2022.
- Wood, A. W., Maurer, E. P., Kumar, A. and Lettenmaier, D. P. (2002) Long-range experimental hydrologic forecasting for the eastern united states. *Journal of Geophysical Research: Atmospheres*, **107**, ACL 6–1–ACL 6–15.
- Xu, S. G. and Reich, B. J. (2021) Bayesian nonparametric quantile process regression and estimation of marginal quantile effects. *Biometrics*, **79**, 151–164.

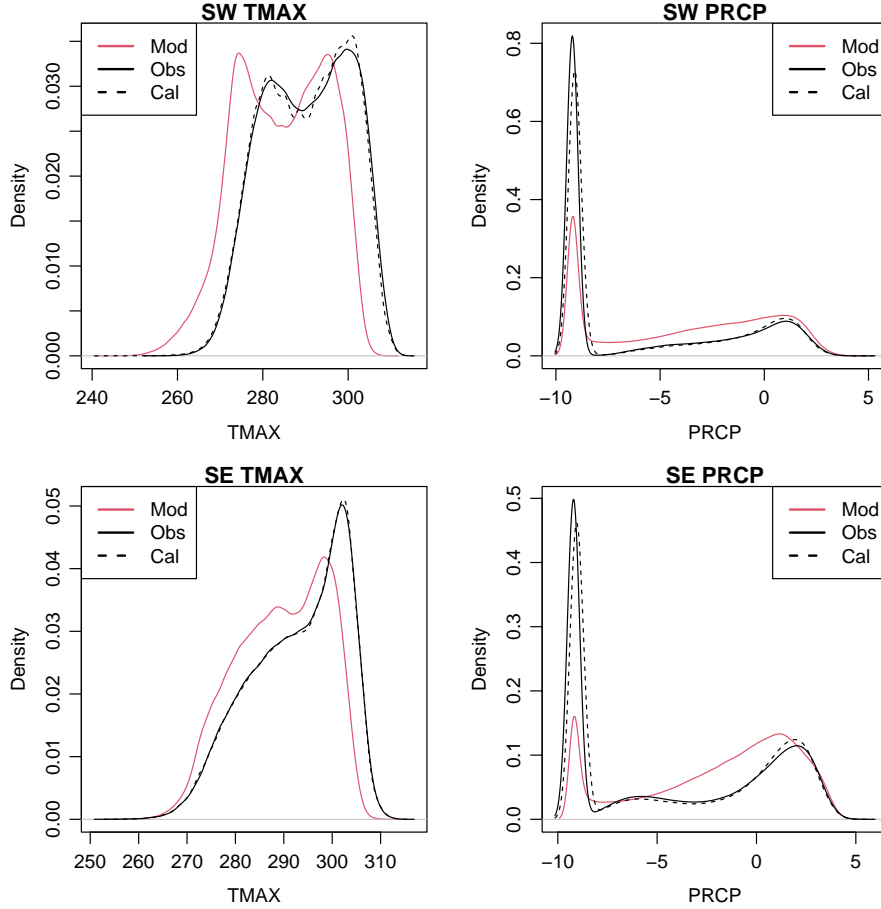


Figure 8: Density curves of TMAX and PRCP data in the Southwest (SW) and Southeast (SE) for 1951–2014 data. PRCP results are presented in the log scale.

A Additional results

In this section, we provide results analogous to Section 3, but focused on in-sample performance. Instead of training the SPCDE on 1951–2000 data, we train it on the entire dataset from 1951–2014. While the focus of this study was the evaluation of SPCDE during the historical period, the eventual goal is future climate projections. In such cases, we would train SPCDE on the entire historical record. The plots and the table provided in this section are identical in all aspects as those provided in Section 3, and only differ in the temporal extent of the data.

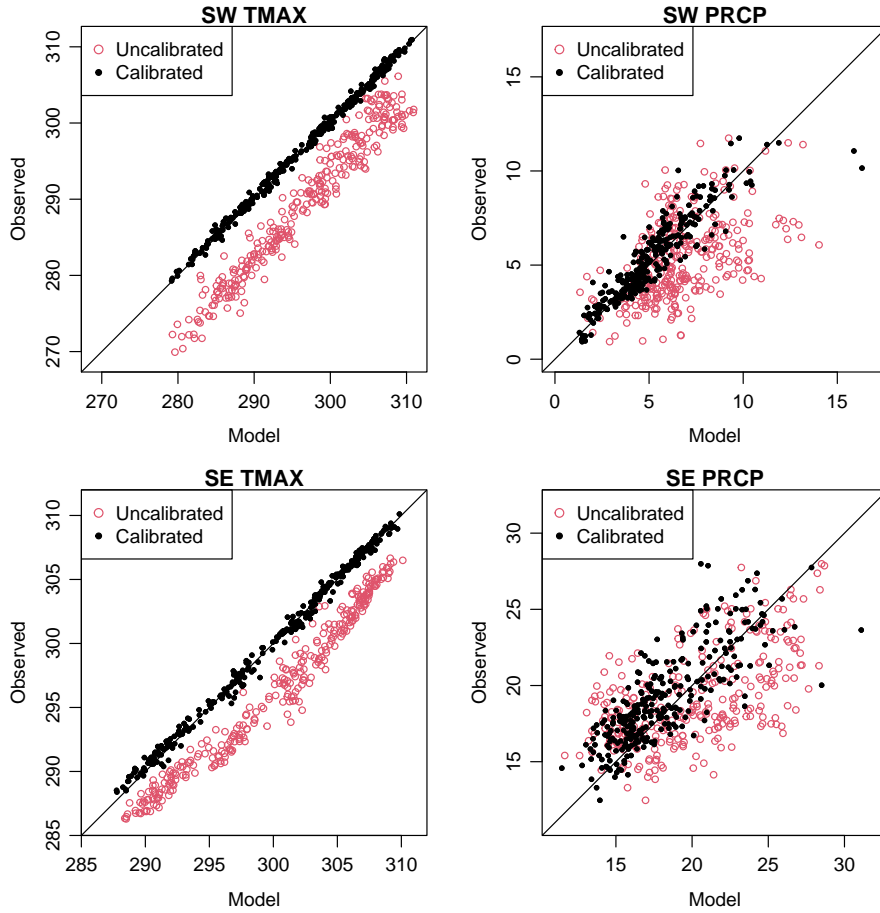


Figure 9: Monthly 0.95 quantiles of TMAX and PRCP data in the Southwest (SW) and Southeast (SE), aggregated over 1951–2014. Each point corresponds to a particular month and location.

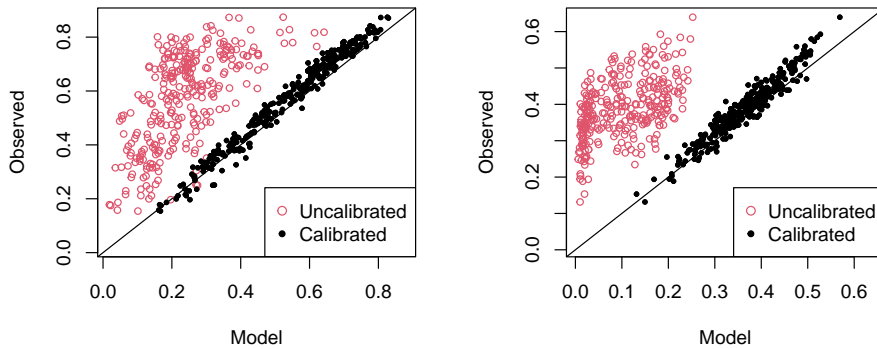


Figure 10: Monthly Proportion of zeros in PRCP data for the Southwest (SW) and Southeast (SE), aggregated over 1951–2014. Each point corresponds to a particular month and location.

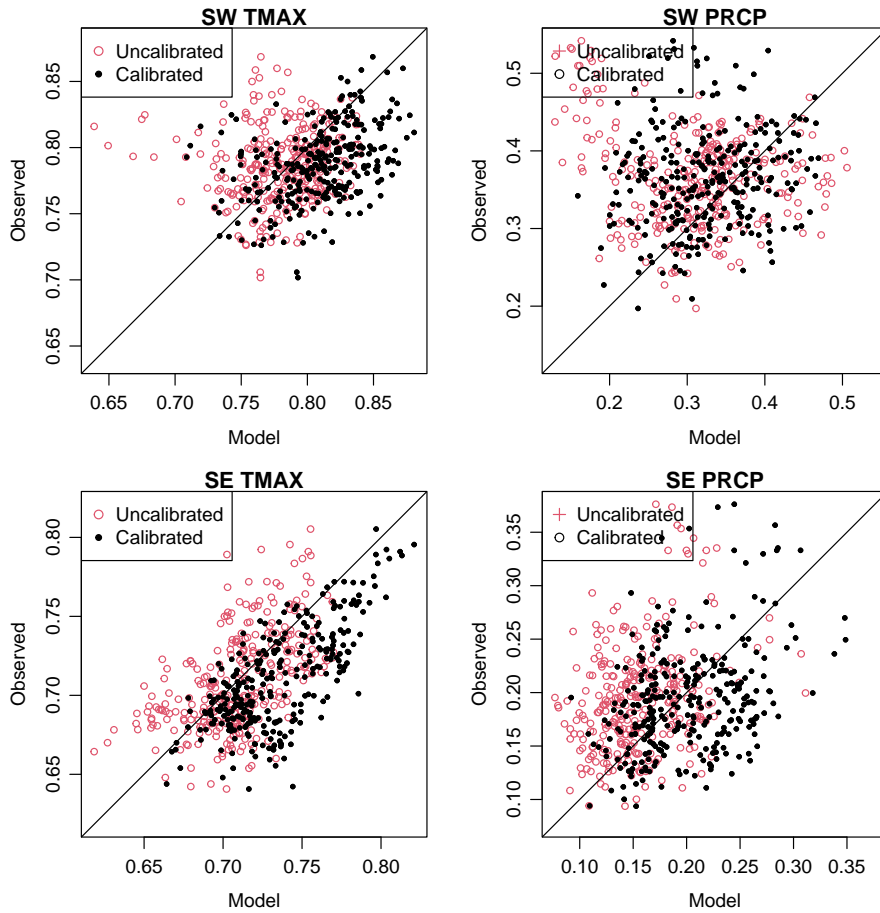


Figure 11: Monthly lag-1 autocorrelations of TMAX and PRCP data in the Southwest (SW) and Southeast (SE), aggregated over 1951–2014. Each point corresponds to a particular month and location.

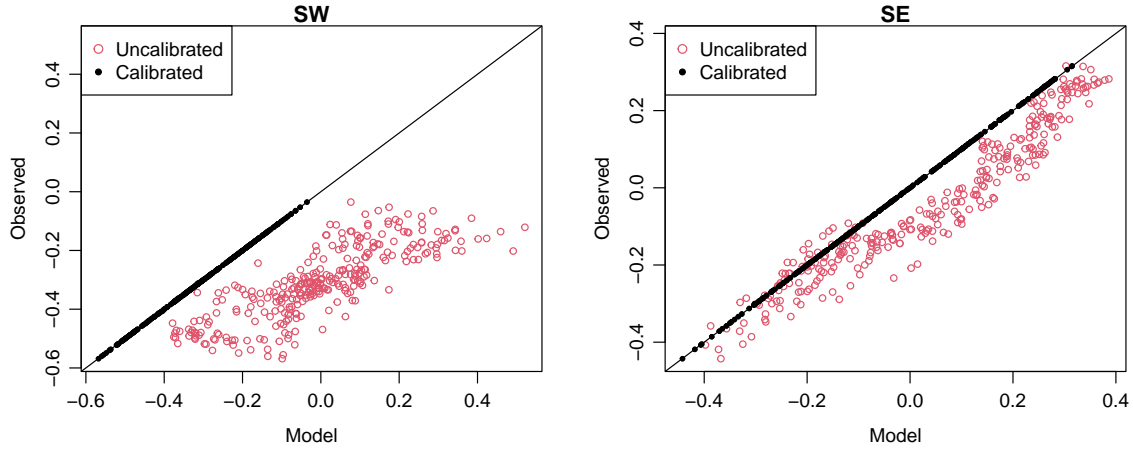


Figure 12: Monthly cross-correlations between TMAX and PRCP in the Southwest (SW) and Southeast (SE), aggregated over 1951–2014. Each point corresponds to a particular month and location.

Table 2: Out-of-sample prediction accuracy in the density correction of TMAX and PRCP based on a spatiotemporal SPQR model, compared with canonical correlation analysis (CCA) and quantile mapping (QM). Other than the Wasserstein distance metric, the remaining values correspond to the RMSE between observed and calibrated data for 1951–2014. Metrics are averaged across spatial locations (pairs of locations for spatial correlation). Best (smallest) values for each combination of region, variable, and metric are highlighted.

		Southwest			Southeast		
		SPQR	CCA	QM	SPQR	CCA	QM
TMAX	Wasserstein distance	0.2673	0.1223	0.1057	0.0747	1.2413	1.2391
	0.95 quantile	0.5617	0.3860	0.3416	0.4488	1.6876	1.6054
	Lag-1 autocorrelation	0.0399	0.0764	0.0357	0.0336	0.0478	0.0297
	Spatial correlation	0.0540	0.0834	0.0709	0.0188	0.0669	0.0579
PRCP	Wasserstein distance	0.0747	0.4083	0.1537	0.2174	0.6851	0.5499
	0.95 quantile	0.9172	0.7263	0.4264	2.2132	2.6586	2.5929
	Proportion of zeros	0.0452	0.2624	0.2172	0.0340	0.1330	0.1722
	Lag-1 autocorrelation	0.0921	0.1461	0.1138	0.0551	0.0878	0.0751
	Spatial correlation	0.0851	0.1951	0.1016	0.0463	0.1334	0.1162
Cross correlation		0.0005	0.3258	0.3258	0.0004	0.0969	0.0969

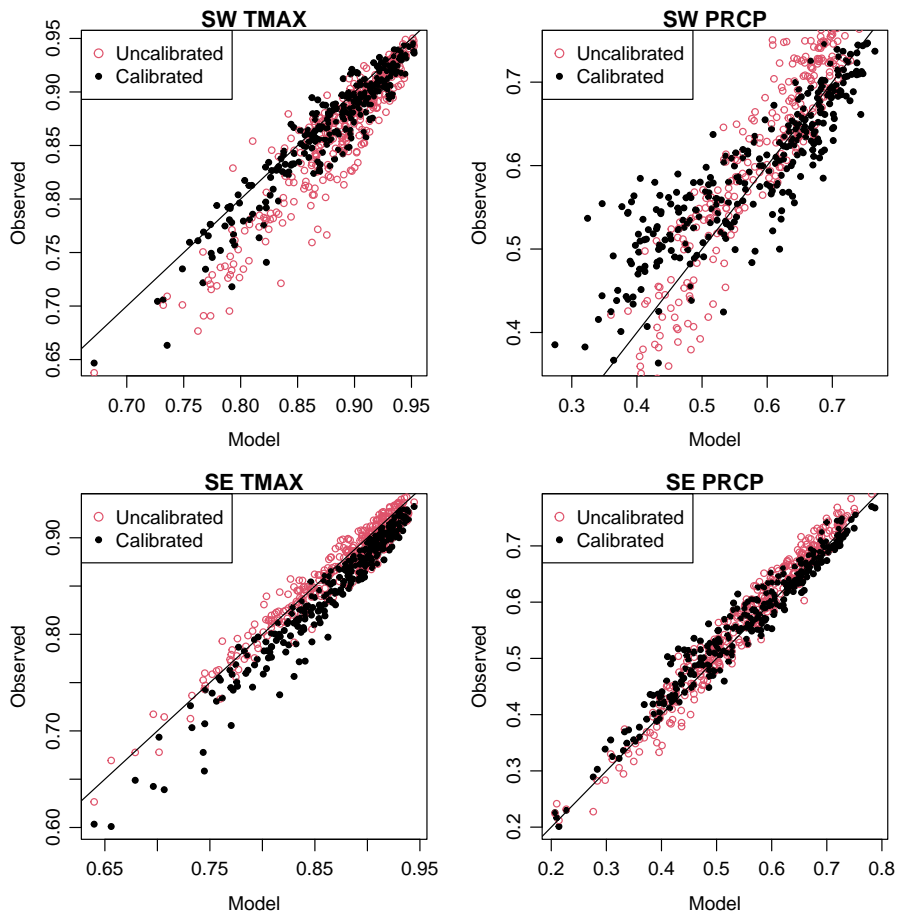


Figure 13: Annual spatial correlations of TMAX and PRCP data in the Southwest (SW) and Southeast (SE), aggregated over 1951–2014. Each point corresponds to a pair of locations.